Controlled Growth of Bismuth Antimony Telluride $Bi_xSb_{2-x}Te_3$ Nanoplatelets and Their Bulk Thermoelectric Nanocomposites

Chaohua Zhang,[1] Zeping Peng, [1,2,*] Zhong Li,[3] Ligen Yu,[3] Khiam Aik Khor,[3] Qihua Xiong[1,*]

[1]*Division of Physics and Applied Physics, School of Physical and Mathematical Science, Nanyang Technological University, 637371 (Singapore)*

[2]*School of Physical Science and Technology, Southwest University, Chongqing 400715 (China)*

[3]*Division of Manufacturing Engineering, School of Mechanical and Aerospace Engineering, Nanyang Technological University, 639798 (Singapore)*

**To whom correspondence should be addressed. E-mail: zppeng@swu.edu.cn and qihua@ntu.edu.sg*

Abstract

Solution synthesis as a scalable bottom-up growth method shows considerable advantages for designing novel nanostructured bulk composites with augmented thermoelectric performance. Tuning the composition of synthesized materials in the solution process is important for adjusting the carrier type and concentration. Here, we report a modified solvothermal synthesis method for the controlled growth of $Bi_xSb_{2-x}Te_3$ nanoplatelets, which can be sintered into nanostructured bulk pellets by using the spark plasma sintering process. We further demonstrate the tuning of the stoichiometric composition in ternary $Bi_xSb_{2-x}Te_3$ nanoplatelets with high crystallinity and homogenous phase purity, which is proved by X-ray diffraction and Raman spectroscopy. The composition dependence of the thermoelectric performance of p-type $Bi_xSb_{2-x}Te_3$ pellets is also systemically studied. The optimized nanostructured bulk $Bi_{0.5}Sb_{1.5}Te_3$ sample is found to have ZT ~0.51 at 375K, which shows great potential for further improving the thermoelectric performance by this solution synthesis method. Considering the progress in n-type Bi-Te-Se composites, our results advocate the promise of bismuth/antimony chalcogenide nanocomposites towards practical thermoelectric applications.

Keywords: Thermoelectricity; $Bi_xSb_{2-x}Te_3$; nanoplatelets; nanostructured composites; Raman; solvothermal synthesis

1. Introduction

Thermoelectric materials are widely used to harvest waste heat to produce useful electricity based on Seebeck effect, or to produce heating or cooling when a current runs through two complementary junctions so-called Peltier effect. To make the practical applications of thermoelectric materials viable, it is crucial to improve the efficiency of thermoelectric materials by enhancing the materials' dimensionless figure of merit (ZT) [1], where $ZT=(S^2\sigma/\kappa)T=(PF/\kappa)T$, and S, σ, κ, T, PF is the thermoelectric power (Seebeck coefficient), electrical conductivity, thermal conductivity, absolute temperature, power factor, respectively. Thus, an ideal thermoelectric material should have large power factor and low thermal conductivity. There have been consecutive efforts in achieving high-ZT thermoelectric materials since 1940s, but the highest ZT in thermoelectric materials had been remained around 1 lasting to the end of last century [2]. The challenge in improving the ZT value is that the parameters S, σ, κ in a material are mutually constrained, for example, increasing S usually leads to a simultaneous decreasing of σ, and increasing the σ leads to the increase of κ at the same time because of the Wiedemann-Franz law [3]. In 1993, Hicks and Dresselhaus predicted that the ZT value could be greatly enhanced in the quantum-well [4] and quantum-wire [5] structures due to enhanced thermoelectric power and the reduced lattice thermal conductivity, which inspires the nanostructuring approach for high-ZT thermoelectric materials. Nanostructuring engineering in bulk alloys has been proven to be an effective strategy to enhance the thermoelectric performance by reducing the lattice thermal conductivity [6-9]. Moreover, band structure engineering strategies have also been proposed to increase the power factor for high thermoelectric performance [10, 11].

Along with the emergence of various new approaches and new materials in the past decade, the ZT values of the bulk materials for high-temperature applications have been greatly improved, such as multiple-filled skutterudites $CoSb_3$ [12], lead antimony silver telluride and its alloy [13], PbTe-based alloys and nanocomposites, [14, 15] and the highest ZT peak has been recorded to be ~2.6 at 923 K for the SnSe

crystal [16]. However, for the low-temperature (about 200-500 K) cooling and power generation applications, Bi_2Te_3-based bulk materials (n-type $Bi_2Te_{3-x}Se_x$ and p-type $Bi_xSb_{2-x}Te_3$) still dominate. Compared with commercial Bi_2Te_3-based alloy ingots, enhanced thermoelectric performances were also observed in nanostructured bulk Bi_2Te_3-based alloys because of the reduced thermal lattice conductivity, which were carried out by various nanostructure engineering approaches such as ball-milling hot-pressing process [17, 18], melt-spinning spark-plasma-sintering process [19], hot forging process [20], and solution-synthesis sintering process [21].

Solution synthesis is a typical bottom-up assembly approach, which is a facile and scalable method to achieve various nanostructures such as nanowires [22], nanobelts [23], nanoplatelets [24, 25], nanonetworks [26], and even heterostructures [27]. Using these nanostructures as building blocks one can harness great possibilities to achieve various novel nanostructured bulk materials for enhancing the thermoelectric performance. However, the solution derived nanostructured bulk materials usually show a low ZT value comparing with the ones made by ball-milling hot-pressing approaches because of the low power factor [28-30], although the lattice thermal conductivity is greatly reduced. For example, a nanostructured bulk Bi_2Te_3 material made from solution synthesized nanoparticles only shows a ZT of 0.04 at room temperature because of the poor electrical conductivity even though the thermal conductivity is as low as 0.51 $Wm^{-1}K^{-1}$ [28]. Thus, to make full advantage of the solution approaches, further systematic controlling on the morphology, structure and composition of nanostructures is greatly needed to optimize the three thermoelectric parameters S, σ, κ for high-ZT bulk nanocomposites. Composition tuning in thermoelectric materials is especially important to adjust the band structure and doping level of the materials for improving the power factor [10]. Up to date, various solution approaches have been widely proposed to synthesize binary Bi_2Te_3 [24, 30, 31] and Sb_2Te_3 [25, 29, 32] nanoplatelets, but the research on the solution synthesis of ternary $Bi_2Te_{3-x}Se_x$ and $Bi_xSb_{2-x}Te_3$ with tunable composition is still limited. Previously we reported the solution synthesis of n-type $Bi_2Te_{3-x}Se_x$ nanoplatelets and

characterizations of the thermoelectric performance of their bulk pellets [33]. In a complete Bi_2Te_3-based thermoelectric device, both n-type $Bi_2Te_{3-x}Se_x$ and p-type $Bi_xSb_{2-x}Te_3$ materials are required. Although some solution approaches have also been reported recently for the synthesis of stoichiometric ternary p-type $Bi_xSb_{2-x}Te_3$ [34, 35], it is still a challenge to improve the power factor of these bulk nanocomposites.

Here, we report a modified solvothermal synthesis method for the controlled growth of $Bi_xSb_{2-x}Te_3$ nanoplatelets, in which the L-cysteine is used as reducing agent to obtain homogenous stoichiometric composition. Using this solution method, the tuning of the stoichiometric composition in ternary $Bi_xSb_{2-x}Te_3$ is successfully realized. Phase segregation problem is overcome by this modified approach. By spark plasma sintering (SPS) of the $Bi_xSb_{2-x}Te_3$ nanoplatelets, the corresponding nanostructured bulk pellets are prepared for thermoelectric characterizations. The optimized nanostructured bulk $Bi_{0.5}Sb_{1.5}Te_3$ sample is found to have ZT ~0.51 at 375K, which shows great potential for further improving the thermoelectric performance by solution synthesis method.

2. Experimental Details

2.1 Sample preparation

In a typical synthesis of $Bi_{0.5}Sb_{1.5}Te_3$ nanoplatelets, 3.26 g potassium telluride monohydrate ($K_2TeO_3 \cdot H_2O$), 0.77 g bismuth acetate ($Bi(OOCCH_3)_3$), 1.79 g antimony acetate ($Sb(OOCCH_3)_3$), 2.24 g KOH and 0.4 g Polyvinylpyrrolidone (PVP) as stabilizing agent were dissolved in the 160 ml diethylene glycol (DEG) solvent with the aid of sonication. To tune the composition *x* in the $Bi_xSb_{2-x}Te_3$, the amount of Bi and Sb precursors also changes following the stoichiometric ratio. The mixed solution were transferred to a 250-mL round bottom flask equipped with a condenser for refluxing. Then 0.8 g L-cysteine was added to the solution and the color changed from white to black immediately. After that, the flask was put on an electrothermal mantel with stirring part. The reaction temperature of the mix solution was set at the

boiling temperature of DEG (~ 240 ^{o}C). The electrothermal mantel power was turned off after heating the blended solution at ~240 ^{o}C for 3 hours, and solution was allowed to cool down to room temperature. The black solution was washed in acetone and isopropyl alcohol with the assistance of sonication and followed by centrifuging. The washing process repeated for several cycles. After that, the $Bi_xSb_{2-x}Te_3$ samples were dried in oven at 60 ^{o}C for 1 hour. Dried $Bi_xSb_{2-x}Te_3$ samples were milled to powders and re-dried at 60 ^{o}C for 0.5 hour.

Dried nano powders were loaded in 10.5 mm (inner diameter) graphite dies and sintered to bulk disk samples (10.5 mm in diameter and 1-2 mm in thickness) using the spark plasma sintering (SPS) system. After pumping the working chamber to a vacuum ~ 5×10^{-02} mbar, the sintering power was turned on to increase the temperature to 350 ^{o}C at a rising rate of 50 ^{o}C/min and maintained for 10 minutes at an applied pressure of 40 MPa. Then the temperature was set to 50 ^{o}C at a decreasing rate of 50 ^{o}C/min, and the applied pressure also decreased to 10 MPa. The densities of the SPS yielded pellets are about 89%-95% of the theoretical densities. After SPS, the bulk samples were cut to bars with length 9-10 mm, width 2-3 mm and thickness 1-2 mm. The bars were polished with sandpapers, and four-probe leads were attached to the bars by applying the silver-filled H20E-HC epoxy.

2.2 Characterization methods

Morphology characterizations of the samples were taken by using scanning electron microscopy (SEM, JEOL 7100F), atomic force microscopy (AFM, scanning probe microscopy model DI dimension V, tapping mode). X-ray diffraction (XRD) patterns were performed using a Bruker D8 advance diffractometer with Cu K_α radiation (λ=0.15404 nm; 40 kV, 40 mA) in the locked couple mode between the X-ray gun and detector. Raman spectroscopy data were collected on a micro-Raman spectrometer (Horiba-JY T64000, 532 nm, 0.07 mW). The temperature dependence of the thermoelectric performances (parameters S, σ, and κ) was measured in a physical properties measurement system (PPMS, Quantum Design) with thermal transport

option, using the timed single mode (each fixed period is set at 2000-3000 s that is long enough to make sure the steady-state measurement at each temperature). Hall measurements were conducted in the same PPMS apparatus using AC transport option. All the thermoelectric measurements were taken along the disc-plane direction that was perpendicular to the SPS-pressing direction.

3. Results and discussions

3.1 Morphology and structure

The synthesized $Bi_xSb_{2-x}Te_3$ nanoplatelets were dropped on SiO_2/Si substrates for morphology characterization. Figure 1(a-g) show the SEM images of the as-grown $Bi_xSb_{2-x}Te_3$ nanoplatelets with different stoichiometric parameters *x*, and all the samples display the hexagonal or the truncated-edge hexagonal morphologies, which are consistent with their layered and rhombohedral crystal structures of the space group $R\bar{3}m$ (D_{3d}^5) [36, 37]. Comparing Figure 1(a) with Figure 1(b-g), the lateral sizes of the binary Sb_2Te_3 nanoplatelets are about ten times larger than that of other ternary $Bi_xSb_{2-x}Te_3$ and binary Bi_2Te_3 nanoplatelets. As shown in the statistical analysis of the lateral size distributions (Supporting information Figure S1), the mean sizes of Sb_2Te_3 (Figure 1(a)) and $Bi_{0.5}Sb_{1.5}Te_3$ (Figure 1(d)) nanoplatelets are 2.8 μm and 240 nm, respectively. And the corresponding thickness of Sb_2Te_3 nanoplatelets is about few tens of nanometers while that of $Bi_{0.5}Sb_{1.5}Te_3$ nanoplatelets is around 10 nm (Supporting information Figure S2). Excluding Sb_2Te_3 nanoplatelets, the size and thickness of other ternary $Bi_xSb_{2-x}Te_3$ and binary Bi_2Te_3 nanoplatelets are in the same level, as shown in Figure 1(b-g). Thus, adding Bi atoms into the lattice of $Bi_xSb_{2-x}Te_3$ greatly reduces the sizes of these nanoplatelets. Because the formation speed of Bi_2Te_3 is much faster than Sb_2Te_3 (Supporting information Figure S3), adding Bi precursors can increase the initial formation rate of ternary $Bi_xSb_{2-x}Te_3$ cluster, which may lead to much more nucleuses for epitaxial growth. Thus more nucleuses will lead to smaller size of nanoplates. After washing and drying, the weight of the collected $Bi_xSb_{2-x}Te_3$ powders can reach above 95% of the theoretical weight, which suggests a

high yield production of $Bi_xSb_{2-x}Te_3$ nano powders using this modified solvothermal synthesis method. Figure 1(h) exhibits a photograph of a $Bi_xSb_{2-x}Te_3$ pellet sample after SPS process, which indicates that this chemical approach has great advantage for scale-up preparations of bulk thermoelectric materials.

To confirm the tuning of stoichiometric parameters *x* in $Bi_xSb_{2-x}Te_3$ nanoplatelets, XRD characterizations were taken on these powder samples, as shown in Figure 2(a-b). The XRD patterns of the as-grown binary Sb_2Te_3 and Bi_2Te_3 samples are well matched with the standard rhombohedral single phase Sb_2Te_3 (PDF-Card 15-0874, lattice parameters $a=b=4.262$ Å, $c=30.45$ Å) and Bi_2Te_3 (PDF-Card 15-0874, lattice parameters $a=b=4.385$ Å, $c=30.48$ Å) respectively, as shown in Supporting information Figure S4. By increasing the Bi composition in $Bi_xSb_{2-x}Te_3$, corresponding XRD peaks for different planes of $Bi_xSb_{2-x}Te_3$ nanoplatelets gradually shift from peaks of the Sb_2Te_3 sample to that of Bi_2Te_3 (Figure 2(a)). Figure 2 (b) shows the enlarge view of the most intense XRD peak for (015) plane, which shows that the 2θ value of these peaks gradually shift from 28.24° to 27.66° as the stoichiometric parameters *x* increases from 0 to 2. The in-plane lattice parameters (*a*, *b*) of $Bi_xSb_{2-x}Te_3$ also shows an appropriate liner dependence on the Bi composition (Supporting information Figure S5). From Sb_2Te_3 to Bi_2Te_3, the increase of in-plane parameters *a*, *b* is about 2.9 % while that of out-plane parameter *c* is only 0.1%. Thus, the adding of Bi components into the layered $Bi_xSb_{2-x}Te_3$ materials mostly influences the distance of the in-plane atoms. After SPS process, the XRD pattern of the prepared pellet is compared with that of synthesized powder, as shown in Figure 2(c). In contrast to the random orientation of the synthesized powder, the XRD patterns of the SPS pellet sample in the plane perpendicular to the press direction (illustrated in inset of Figure 2(c)) show preferential orientation, in agreement with previous report. [38] The SPS pellet shows much stronger diffraction intensities of the (006) and (0015), which clearly demonstrate that the reorientation of *ab* planes of nanoplatelets into the disc plane during the SPS process. The reorientation phenomenon is also presented in ball-milling hot-pressing derived bulk samples [18], which shows positive influence

on the thermoelectric performance.

To further prove the substitution of Sb atoms by Bi atoms in $Bi_xSb_{2-x}Te_3$ systems, Raman spectroscopy of $Bi_xSb_{2-x}Te_3$ nanoplatelets was taken to investigate the composition dependence of the phonon frequencies, as shown in Figure 3(a). As demonstrated by the XRD above, layered Sb_2Te_3, Bi_2Te_3 and $Bi_xSb_{2-x}Te_3$ nanoplatelets have the rhombohedral crystal structure, which are composed of *ab*-plane hexagonal close-packed atomic layers, periodically stacking along the *c*-axis. In the *c*-axis direction, the atomic arrangements can be considered as the repeating stacking of quintuple-layers stacked by van der Waal's force [36]. Taking Sb_2Te_3 as a typical example, each quintuple-layer consists of five atomic layers arranged as Te(1)-Sb-Te(2)-Sb-Te(1), in which Te atoms show two different chemical environments (marked as Te(1) and Te(2)), as illustrated in Figure 3(b). Three kinds of peaks are clearly shown in the Raman spectra of different $Bi_xSb_{2-x}Te_3$ nanoplatelets, which are A_{1g}^1 (60-70 cm^{-1}), E_g^2 (100-115 cm^{-1}) and A_{1g}^2 (130-170 cm^{-1}), as shown in Figure 3(a). Figure 3(b) shows the schematic draw of the linear-chain vibration modes for the three Raman active phonons modes (A_{1g}^1, E_g^2 and A_{1g}^2), which are two out-of-plane modes (A_{1g}^1 and A_{1g}^2) and one in-plane mode (E_g^2). As shown in Figure 3(c), with the substitution of Sb atoms by Bi atoms in $Bi_xSb_{2-x}Te_3$ systems, there is a continuous variation of the three Raman modes, which gradually shift from peaks of Sb_2Te_3 (A_{1g}^1~ 70 cm^{-1}, E_g^2~113 cm^{-1} and A_{1g}^2~165 cm^{-1}) to that of Bi_2Te_3 (A_{1g}^1~ 62 cm^{-1}, E_g^2~103 cm^{-1} and A_{1g}^2~139 cm^{-1}). The Raman peaks of as-grown Bi_2Te_3 and Sb_2Te_3 nanoplatelets agree well with other reported samples [37, 39]. The continuous composition dependence of the Raman modes in $Bi_xSb_{2-x}Te_3$ nanoplatelets is also consistent with $Bi_xSb_{2-x}Te_3$ crystals synthesized by Bridgman technique [36], which indicates that uniform composition tuning of ternary $Bi_xSb_{2-x}Te_3$ nanoplatelets is realized by our modified solvothermal synthesis method.

As proved by the XRD and Raman characterizations above, the composition of our as-grown $Bi_xSb_{2-x}Te_3$ nanoplatelets can be homogenously tuned. L-cysteine plays a crucial role to obtain homogenous composition in this modified sovothermal

synthesis. Control experiments without adding L-cysteine resulted in two separated phases Bi_2Te_3 and Sb_2Te_3 rather than a single phase $Bi_xSb_{2-x}Te_3$ nanoplatelets (Supporting information Figure S6). In addition, without L-cysteine the growth speed of Sb_2Te_3 is much slower than that of Bi_2Te_3 (Supporting information Figure S3), which can be the reason for the separated phases. By replacing L-cysteine with another normally used reducing agent L-ascorbic acid, single phase $Bi_xSb_{2-x}Te_3$ nanoplatelets can also be achieved, however the lateral size is much smaller and the morphology is less uniform than that of as-growth samples with adding L-cysteine (Supporting information Figure S7). Thus, L-cysteine serves as both reducing and stabilizing agent. As observed in the synthesis process, the color of the solution changed from white to black immediately when L-cysteine was added, which indicates its strong reducing nature. Compared with other commonly used reducing agent such as sodium borohydride ($NaBH_4$) [25] and hydrazine hydrate ($N_2H_4{\cdot}H_2O$) [32] in the solution synthesis of Sb_2Te_3 nanoplatelets, L-cysteine is much safer for scale-up chemical synthesis process.

3.2 Thermoelectric performances

The as-grown $Bi_xSb_{2-x}Te_3$ nanopowders were made into disk-like bulk pellets by SPS approach, and these pellets were cut into rectangular bars for thermoelectric characterization. Figure 4 shows the temperature-dependent thermoelectric properties of the $Bi_xSb_{2-x}Te_3$ pellets with various compositions, and Figure 5 summarizes the composition dependence of thermoelectric properties at 300 K. All the properties were measured in the same disc-plane direction with the four-probe device configuration. As shown in Figure 4(a), the electrical conductivity of the $Bi_xSb_{2-x}Te_3$ pellets decreases as the temperature increases from 20 K to 375 K, which indicates that all the samples have metallic behaviors. The electrical conductivity also shows dependence on the composition of $Bi_xSb_{2-x}Te_3$. The Sb_2Te_3 pellet has an electrical conductivity of about 1.5×10^5 S/m at 300 K, which is higher than those p-type ternary $Bi_xSb_{2-x}Te_3$ pellets (range from 0.4×10^5 S/m to 1.2×10^5 S/m at 300 K). The reason for the decrease of electrical conductivity in the ternary $Bi_xSb_{2-x}Te_3$ pellets

could be the enhancing of the electron scattering when more Bi atoms substitute Sb atoms in the lattice. Nevertheless, the electrical conductivities of our p-type $Bi_xSb_{2-x}Te_3$ samples are higher than that of other solution derived samples [34, 35] and comparable with that of p-type alloy ingot that is on the level of 1×10^5 S/m at 300 K [17].

As shown in Figure 4(b), the thermoelectric power *S* for all the $Bi_xSb_{2-x}Te_3$ pellets with Bi composition from x=0 to x=0.8 has positive values in the test temperature range 20 K-375 K, showing a typical p-type behavior. However, when the Bi composition x in $Bi_xSb_{2-x}Te_3$ pellets is larger than 1, the $Bi_xSb_{2-x}Te_3$ pellets can have negative thermoelectric power, revealing the n-type behavior, as summarized in Figure 5(a). As the n-type thermoelectric performance of $Bi_xSb_{2-x}Te_3$ pellets is much lower than our previous n-type $Bi_2Te_{3-x}Se_x$ pellets, this work focus on the tuning and thermoelectric characterization of p-type $Bi_xSb_{2-x}Te_3$ pellets. As shown in Figure 4(b), the thermoelectric power value of all the p-type pellets increases with the increasing temperature from 20 K to 375 K, showing nearly linear temperature dependence. Using a simple parabolic band structure and energy-independent scattering approximation, the thermoelectric power *S* is usually given by [3]:

$$S = \frac{\pi^2 k_B^2 T}{3e} \frac{d \ln \sigma(E)}{dE}\Big|_{E=E_F} = \frac{8\pi^2 k_B^2}{3eh^2} m^* (\frac{\pi}{3n})^{2/3} \mathrm{T}$$

where k_B, e, h, m^*, n is the Boltzmann constant, electronic charge, Planck's constant, effective mass of electrons, carrier density, respectively. Thus, the slope of the temperature dependence of thermoelectric power is mostly determined by the effective mass of electrons m^* and carrier density *n*. Hall measurements reveal that charge-carrier concentration varies in the range $1\text{-}9\times10^{19}$ cm^{-3}, carrier mobility in the range 40-340 $cm^2V^{-1}s^{-1}$ by varying the composition (Supporting information Table S1), which are comparable to other nanostructured bulk $Bi_xSb_{2-x}Te_3$. As shown in Figure 4(b) and Figure 5(a), the thermoelectric power of the $Bi_xSb_{2-x}Te_3$ pellets is adjusted by tuning the Bi composition, which suggests that the control of the composition in $Bi_xSb_{2-x}Te_3$ pellets is an effective way to tune the effective mass of

electrons m^* and carrier density n. Figure 5(a) shows the composition dependence of thermoelectric power at 300 K, and the value of thermoelectric power increases from 91 μV/K for binary Sb_2Te_3 pellet to 168 μV/K for $Bi_{0.5}Sb_{1.5}Te_3$ pellet. The maximum S is reached to ~ 193 μV/K for $Bi_{0.5}Sb_{1.5}Te_3$ pellet at 375 K. Figure 4(c) shows the temperature dependence of power factor ($S^2\sigma$) for $Bi_xSb_{2-x}Te_3$ pellets, which is derived from Figure 4(a) and 4(b). As the S and σ show opposite temperature dependence, the power factors of these pellets can increase at low temperatures range and decrease at high temperature range, reaching a maximum value at medium temperature. The composition dependence of power factor is displayed in Figure 5(b). The maximum power factor at 300 K we have achieved at present is about 18 $\mu Wcm^{-1}K^{-2}$ for the $Bi_{0.2}Sb_{1.8}Te_3$ pellet, which is much higher than other solution-derived samples with maximum power factor 1-9 $\mu Wcm^{-1}K^{-2}$ [34, 35], but it is still about 2.5 times smaller than the maximum power factor of the state-of-art p-type $Bi_xSb_{2-x}Te_3$ alloy ingot [17]. Further efforts are still demanded in order to optimize the Seebeck coefficient and the electrical conductivity for higher thermoelectric performance.

Reducing the thermal conductivity by nanostructuring has been widely reported for enhancing the thermoelectric performance. Figure 4(d) shows the temperature dependence of the thermal conductivity for $Bi_xSb_{2-x}Te_3$ pellets, which were measured using the four-probe steady-state method on the PPMS. All the $Bi_xSb_{2-x}Te_3$ pellets show similar temperature dependence of thermal conductivity from 20 K to 375 K, which increases in low temperature range and decreases in high temperature range, and each sample has a maximum thermal conductivity at about 50-100 K. The measured thermal conductivity has contributions from the phonons and charge carrier. The contribution from phonons (lattice vibrations) is the lattice thermal conductivity κ_l and the contribution from charge carriers (electrons or holes) is electronic thermal conductivity κ_e. According to the Wiedemann-Franz law, the electronic thermal conductivity is related to the electrical conductivity, $\kappa_e = L\sigma T$, where L is the Lorenz number. The Lorenz number $L = 2.45 \times 10^{-8}$ $W\Omega K^{-1}$ is usually taken for metals and degenerate semiconductors [8]. Giving the electrical conductivity in Figure 4(a)

and the total thermal conductivity in Figure 4(d), we plotted the temperature dependence of lattice thermal conductivity by the formula $\kappa_l = \kappa_{total} - \kappa_e = \kappa_{total} - L\sigma T$, which is displayed in Figure 4(e). As shown in Figure 4(e), the lattice thermal conductivity shows increasing trend in the low temperature range, which is caused by the excitation of phonons. When enough phonons are excited at high temperature, the phonon-phonon scattering dominates due to the *Umklapp* process, which leads to the decrease of lattice thermal conductivity at high temperature following 1/T temperature dependence. As shown in Figure 4(e), each $Bi_xSb_{2-x}Te_3$ pellets has the lowest lattice thermal conductivity at 375 K, which is in the range 0.2-1 $Wm^{-1}K^{-1}$. Figure 5(c) displays the composition dependence of the lattice thermal conductivity for $Bi_xSb_{2-x}Te_3$ pellets at 300 K, which is in the range 0.4-1 $Wm^{-1}K^{-1}$. The lattice thermal conductivity we achieved at present is comparable with the previous reported nanostructured bulk Bi_2Te_3-based materials [17, 21].

Figure 4(f) shows the temperature dependence of Figure of merit (ZT) for $Bi_xSb_{2-x}Te_3$ pellets, which is calculated basing on the formula $ZT=(S^2\sigma/\kappa)T$. Increasing the temperature from 20 K to 375 K, the ZT value for all the pellets shows increasing trend with no peaks in this temperature range. Figure 5(d) shows the composition dependence of the ZT value for $Bi_xSb_{2-x}Te_3$ pellets at 300 K, which suggests the tuning of ZT value by composition control. The maximum ZT value we achieved at present is about 0.51 for $Bi_{0.5}Sb_{1.5}Te_3$ pellets at 375 K. Our $Bi_xSb_{2-x}Te_3$ pellets show relatively low lattice thermal conductivity, so the bottleneck is that the power factor is still low. We ascribed the low power factor of our samples to the influence of some residual chemicals or molecules absorbed on the surface of $Bi_xSb_{2-x}Te_3$ nanoplatelets, and further improvement of the power factor may be realized by using appropriate surface treatment [26].

4. Conclusions

In summary, we have developed a modified solvothermal synthesis to grow $Bi_xSb_{2-x}Te_3$ nanoplatelets with excellent control of composition tenability and

crystalline quality. Nanostructured bulk $Bi_xSb_{2-x}Te_3$ pellets are made from spark plasma sintering of the corresponding nanopowders, which demonstrate the tuning of thermoelectric properties by varying the composition. The p-type $Bi_xSb_{2-x}Te_3$ pellets show low lattice thermal conductivity, though the power factor is still a little lower than state-of-art $Bi_xSb_{2-x}Te_3$ alloy ingot. The ZT value of optimized $Bi_{0.5}Sb_{1.5}Te_3$ pellet reaches to 0.51 at 375 K. The realization of composition control in p-type $Bi_xSb_{2-x}Te_3$ by this bottom-up solution method opens up great possibilities for future designing of novel nanostructures to lift up the thermoelectric performance. In addition, complete thermoelectric devices for practical applications can be realized by combing our p-type $Bi_xSb_{2-x}Te_3$ with previous reported n-type $Bi_2Te_{3-x}Se_x$.

Acknowledgements

Q.X. gratefully thanks Singapore National Research Foundation via a Fellowship grant (NRF-RF2009-06) and an Investigatorship grant (NRF-NRFI2015-03), Ministry of Education via a tier2 grant (MOE2012-T2-2-086) and Nanyang Technological University via a start-up grant support (M58110061).

Additional Information

Supplementary Information is available online

References

[1] L.E. Bell, Science 321 (2008) 1457-1461.
[2] J.P. Heremans, M.S. Dresselhaus, L.E. Bell, D.T. Morelli, Nature nanotechnology 8 (2013) 471-473.
[3] G.J. Snyder, E.S. Toberer, Nature materials 7 (2008) 105-114.
[4] L. Hicks, M. Dresselhaus, Physical Review B 47 (1993) 12727-12731.
[5] L. Hicks, M. Dresselhaus, Physical Review B 47 (1993) 16631-16634.
[6] M.G. Kanatzidis, Chemistry of Materials 22 (2010) 648-659.
[7] W. Liu, X. Yan, G. Chen, Z. Ren, Nano Energy 1 (2012) 42-56.
[8] J.R. Sootsman, D.Y. Chung, M.G. Kanatzidis, Angew Chem Int Ed Engl 48 (2009) 8616-8639.
[9] A.J. Minnich, M.S. Dresselhaus, Z.F. Ren, G. Chen, Energy & Environmental Science 2 (2009) 466.
[10] Y. Pei, H. Wang, G.J. Snyder, Advanced materials 24 (2012) 6125-6135.
[11] J.P. Heremans, B. Wiendlocha, A.M. Chamoire, Energy & Environmental Science 5 (2012) 5510.
[12] X. Shi, J. Yang, J.R. Salvador, M. Chi, J.Y. Cho, H. Wang, S. Bai, J. Yang, W. Zhang, L. Chen, Journal of the American Chemical Society 133 (2011) 7837-7846.
[13] K.F. Hsu, S. Loo, F. Guo, W. Chen, J.S. Dyck, C. Uher, T. Hogan, E.K. Polychroniadis, M.G. Kanatzidis, Science 303 (2004) 818-821.
[14] K. Biswas, J. He, I.D. Blum, C.I. Wu, T.P. Hogan, D.N. Seidman, V.P. Dravid, M.G. Kanatzidis, Nature 489 (2012) 414-418.
[15] Y. Pei, X. Shi, A. LaLonde, H. Wang, L. Chen, G.J. Snyder, Nature 473 (2011) 66-69.
[16] L.D. Zhao, S.H. Lo, Y. Zhang, H. Sun, G. Tan, C. Uher, C. Wolverton, V.P. Dravid, M.G. Kanatzidis, Nature 508 (2014) 373-377.
[17] B. Poudel, Q. Hao, Y. Ma, Y. Lan, A. Minnich, B. Yu, X. Yan, D. Wang, A. Muto, D. Vashaee, X. Chen, J. Liu, M.S. Dresselhaus, G. Chen, Z. Ren, Science 320 (2008) 634-638.
[18] X. Yan, B. Poudel, Y. Ma, W.S. Liu, G. Joshi, H. Wang, Y. Lan, D. Wang, G. Chen, Z.F. Ren, Nano letters 10 (2010) 3373-3378.
[19] W. Xie, J. He, H.J. Kang, X. Tang, S. Zhu, M. Laver, S. Wang, J.R. Copley, C.M. Brown, Q. Zhang, T.M. Tritt, Nano letters 10 (2010) 3283-3289.
[20] J.-J. Shen, T.-J. Zhu, X.-B. Zhao, S.-N. Zhang, S.-H. Yang, Z.-Z. Yin, Energy & Environmental Science 3 (2010) 1519-1523.
[21] R.J. Mehta, Y.L. Zhang, C. Karthik, B. Singh, R.W. Siegel, T. Borca-Tasciuc, G. Ramanath, Nature materials 11 (2012) 233-240.
[22] G. Zhang, B. Kirk, L.A. Jauregui, H. Yang, X. Xu, Y.P. Chen, Y. Wu, Nano letters 12 (2012) 56-60.
[23] W.D. Shi, J.B. Yu, H.S. Wang, H.J. Zhang, Journal of the American Chemical Society 128 (2006) 16490-16491.
[24] W.G. Lu, Y. Ding, Y.X. Chen, Z.L. Wang, J.Y. Fang, Journal of the American Chemical Society 127 (2005) 10112-10116.
[25] W.Z. Wang, B. Poudel, J. Yang, D.Z. Wang, Z.F. Ren, Journal of the American Chemical Society 127 (2005) 13792-13793.
[26] W. Liu, C.F. Guo, M. Yao, Y. Lan, H. Zhang, Q. Zhang, S. Chen, C.P. Opeil, Z. Ren, Nano Energy 4 (2014) 113-122.
[27] H. Yang, J.H. Bahk, T. Day, A.M. Mohammed, G.J. Snyder, A. Shakouri, Y. Wu, Nano letters (2015).
[28] M.R. Dirmyer, J. Martin, G.S. Nolas, A. Sen, J.V. Badding, Small 5 (2009) 933-937.
[29] G.-H. Dong, Y.-J. Zhu, L.-D. Chen, Journal of Materials Chemistry 20 (2010) 1976.

[30] J. Fu, S. Song, X. Zhang, F. Cao, L. Zhou, X. Li, H. Zhang, CrystEngComm 14 (2012) 2159.
[31] J.S. Son, M.K. Choi, M.K. Han, K. Park, J.Y. Kim, S.J. Lim, M. Oh, Y. Kuk, C. Park, S.J. Kim, T. Hyeon, Nano letters 12 (2012) 640-647.
[32] W. Shi, L. Zhou, S. Song, J. Yang, H. Zhang, Advanced materials 20 (2008) 1892-1897.
[33] A. Soni, Z. Yanyuan, Y. Ligen, M.K. Aik, M.S. Dresselhaus, Q. Xiong, Nano letters 12 (2012) 1203-1209.
[34] M. Scheele, N. Oeschler, I. Veremchuk, K.G. Reinsberg, A.M. Kreuziger, A. Kornowski, J. Broekaert, C. Klinke, H. Weller, Acs Nano 4 (2010) 4283-4291.
[35] Y.X. Zhao, J.S. Dyck, B.M. Hernandez, C. Burda, Journal of the American Chemical Society 132 (2010) 4982-+.
[36] W. Richter, H. Kohler, C.R. Becker, Physica Status Solidi B-Basic Research 84 (1977) 619-628.
[37] K.M.F. Shahil, M.Z. Hossain, V. Goyal, A.A. Balandin, Journal of Applied Physics 111 (2012) 054305.
[38] A. Soni, Y. Shen, M. Yin, Y. Zhao, L. Yu, X. Hu, Z. Dong, K.A. Khor, M.S. Dresselhaus, Q. Xiong, Nano letters 12 (2012) 4305-4310.
[39] Y. Zhao, X. Luo, J. Zhang, J. Wu, X. Bai, M. Wang, J. Jia, H. Peng, Z. Liu, S.Y. Quek, Q. Xiong, Physical Review B 90 (2014) 245428.

Figure and Figure Legends

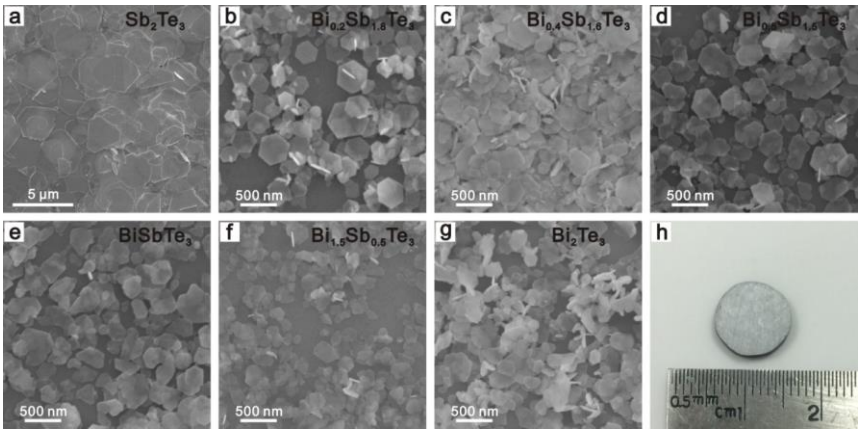

Figure 1 Morphology characterizations of $Bi_xSb_{2-x}Te_3$. SEM images of the as-grown (a) Sb_2Te_3, (b) $Bi_{0.2}Sb_{1.8}Te_3$, (c) $Bi_{0.4}Sb_{1.6}Te_3$, (d) $Bi_{0.5}Sb_{1.5}Te_3$, (e) $BiSbTe_3$, (f) $Bi_{1.5}Sb_{0.5}Te_3$ and (g) Bi_2Te_3 nanoplatelets -on SiO_2/Si substrate. (h) A photograph of a pellet samples after spark plasma sintering process.

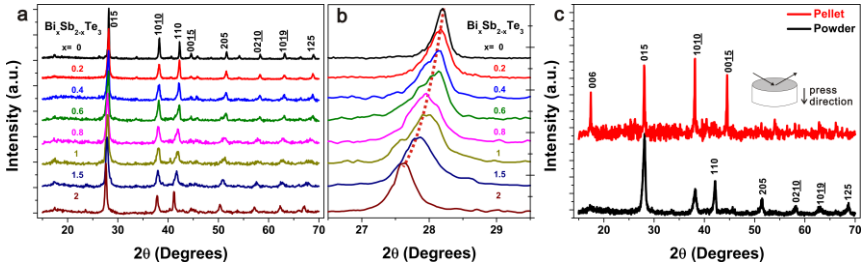

Figure 2 XRD characterization of $Bi_xSb_{2-x}Te_3$. (a)(b) XRD patterns of $Bi_xSb_{2-x}Te_3$ powders with different Bi composition. (b) is the enlarge view of (015) peak shown in (a), showing the peak shift with the change of Bi composition. (c) XRD spectra of the synthesized $Bi_{0.5}Sb_{1.5}Te_3$ powder and pellet. The inset of (c) shows the detected surface of the as-pressed pellet perpendicular to the press direction.

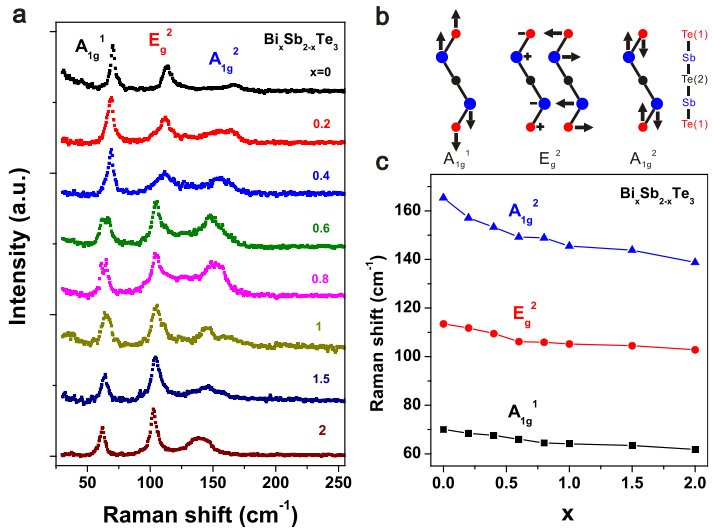

Figure 3 Raman characterizations of $Bi_xSb_{2-x}Te_3$ nanoplatelets. (a) Raman spectra of $Bi_xSb_{2-x}Te_3$ nanoplatelets with different Bi composition. The nanoplatelets are deposited on SiO_2/Si substrate. (b) Schematic draws of the three Raman active modes (A_{1g}^1, E_g^2, A_{1g}^2) of Sb_2Te_3. (c) Phonon frequencies plotted versus the composition parameter *x* of $Bi_xSb_{2-x}Te_3$.

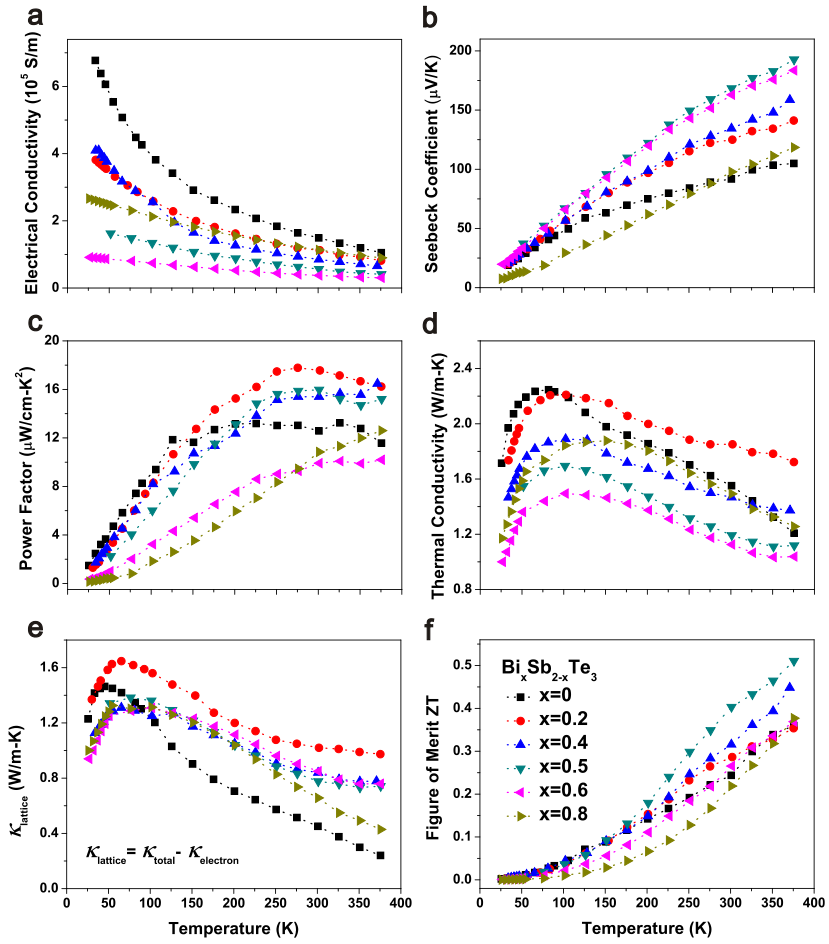

Figure 4 Thermoelectric performance of $Bi_xSb_{2-x}Te_3$ pellets. Temperature dependence of (a) electrical conductivity, (b) Seebeck coefficient, (c) power factor, (d) thermal conductivity, (e) lattice thermal conductivity, and (f) figure of merit ZT of $Bi_xSb_{2-x}Te_3$ pellets with different composition parameter *x*. All the figures share the same annotation as shown in (f).

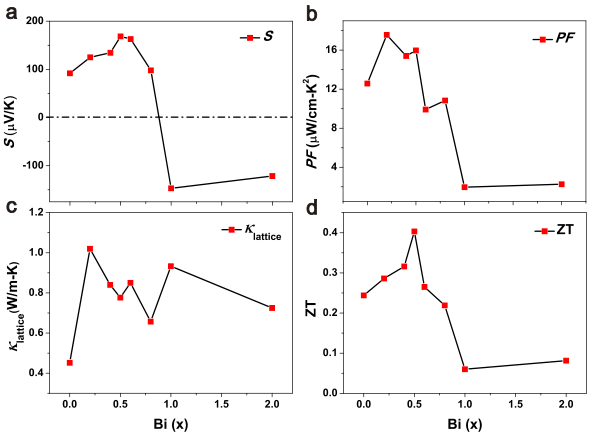

Figure 5 Composition parameter *x* dependence of (a) Seebeck coefficient, (b) power factor, (c) lattice thermal conductivity, and (d) figure of merit ZT of $Bi_xSb_{2-x}Te_3$ pellets at 300K.